Iraqi Journal of Physics, 2023
https://doi.org/10.30723/ijp.v21i3.1153
Vol. 21 No. 3, PP. 41-54
P-ISSN: 2070-4003
E-ISSN: 2664-5548

Influence of DC Magnetron Sputtering Power on Structural, Topography, and Gas Sensor Properties of Nb_2O_5/Si Thin Films

Yahya R. Hathal[1a *], Isam M. Ibrahim[1b], Mohammed K. Khalaf [2c], Ehsan H. Sabbar[3d] and Musaria K. Mahmood[4e]
[1]*Department of Physics, College of Science, University of Baghdad, Baghdad, Iraq*
[2]*Materials Research Department, Ministry of Science and Technology, Baghdad, Iraq*
[3]*Department of Electrical Engineering, University of Anbar, Ramadi, Iraq*
[4]*Department of Energy Systems Engineering, Ankara Yildirim Beyazit University, Turkey*
[b]E-mail: Isam.ibrahim@sc.uobaghdad.edu.iq, [c]E-mail: mohammedkhkh@yahoo.com,
[d]E-mail: Ehsan.sabbar@uoanbar.edu.iq, [e]E-mail: mkmahmood@aybu.edu.tr
[a*]Corresponding author: yahia.rasheed1104a@sc.uobaghdad.edu.iq

Abstract

This study focuses on synthesizing Niobium pentoxide (Nb_2O_5) thin films on silicon wafers and quartz substrates using DC reactive magnetron sputtering for NO_2 gas sensors. The films undergo annealing in ambient air at 800 °C for 1 hr. Various characterization techniques, including X-ray diffraction (XRD), atomic force microscopy (AFM), energy-dispersive X-ray spectroscopy (EDS), Hall effect measurements, and sensitivity measurements, are employed to evaluate the structural, morphological, electrical, and sensing properties of the Nb_2O_5 thin films. XRD analysis confirms the polycrystalline nature and hexagonal crystal structure of Nb_2O_5. The optical band gap values of the Nb_2O_5 thin films demonstrate a decrease from 4.74 to 3.73 eV as the sputtering power is increased from 25 to 75 W. AFM images illustrate a progressive increase in particle size ranging from (41.86) to (45.56) nm, with varying sputtering power between 25 and 75 W. Additionally, EDS analysis validates the rise in Nb content, increasing from 12.2 at. % to 20.1 at. %, corresponding to the increase in sputtering power. Hall effect measurements show that all films exhibit n-type charge carriers, and increasing sputtering power leads to decreased carrier concentration and enhanced mobility. The gas sensor's sensitivity, response, and recovery time were evaluated at various operating temperatures. The NO_2 sensor exhibited an optimal sensitivity of 28.6% at 200 °C when the sputtering power was set to 50 W.

Article Info.

Keywords:
Nb_2O_5, sputtering, EDX, sensitivity, NO_2.

Article history:
Received: Jun. 20, 2023
Revised: Jul. 30, 2023
Accepted: Aug.13, 2023
Published: Sep.01,2023

1. Introduction

Nb_2O_5 stands for niobium pentoxide, a chemical compound composed of two niobium (Nb) atoms and five oxygen (O) atoms. It is an oxide of niobium and exists in a solid state as a white or light-yellow powder. Nb_2O_5 is a metal oxide with various applications in areas such as gas sensors and catalysis [1-3]. Nb_2O_5 films exhibit exceptional optical and structural characteristics that make them highly desirable in various applications [4, 5]. These properties include a high refractive index, low optical absorption, corrosion resistance, thermal stability, and chemical stability [6, 7]. The films find applications in optical waveguides, coatings, filters, electrochromic devices, biosensors, solar cells, and more [8, 9]. In particular, there is growing interest in Nb_2O_5 films for their electrochromic properties, which are influenced by their crystal structure. Factors such as stoichiometry, crystal structure, and surface roughness play a significant role in determining the optical and structural properties of the films. Understanding and controlling these parameters are essential for optimizing the performance of Nb_2O_5 films in electrochromic devices and other applications [10].

NO_2 is a volatile and hazardous gas with a strong odor, posing significant risks to human health and the environment. It is produced by various sources, such as vehicle exhaust, fossil fuel combustion, and industrial emissions [11, 12]. NO_2 can undergo

photochemical reactions, leading to the formation of ozone and acid rain. It can cause discomfort, coughing, eye irritation, fatigue, and nausea, even at low concentrations. Furthermore, it can adversely affect the respiratory system, potentially causing pulmonary diseases without noticeable symptoms. Detecting NO_2 has become crucial due to its harmful impact on human health and the environment [13]. The initial Nb_2O_5 gas sensors for O_2 were introduced by Kondo et al. in 1983 [14]. Subsequently, in 1999, Chambon et al. [15] presented a gas sensor incorporating the nanostructured form of Nb_2O_5. Since then, Nb_2O_5 has been extensively investigated for gas-sensing applications, including O_2, H_2, CO, NH_3, and various hydrocarbons (HCs) [16].

Various methods have been employed to deposit Nb_2O_5 thin films, encompassing techniques such as DC/RF plasma magnetron sputtering, ion beam sputtering (IBS), electron beam evaporation, thermal oxidation, photochemical vapor deposition, plasma-enhanced chemical vapor deposition (PECVD), spray pyrolysis, sol-gel techniques, and pulsed laser deposition (PLD) [17-22]. Sputtering is recognized for its capability to achieve rapid deposition rates, uniform film distribution, consistent composition, high density, purity, and strong adhesion properties. It provides reliable results and allows for the consistent deposition of thin films with even thickness on large substrates. Furthermore, commercially available sputtering systems make it easy to deposit thin films that demonstrate both exceptional transparency and conductivity [23-25]. DC sputtering at low pressure is a fundamental and cost-effective method for Physical Vapor Deposition (PVD) of metal and electrically conductive target coating materials [26]. The DC process offers two notable advantages for coating applications: easy controllability and affordability, though its material selection is limited to metals only [27, 28]. This technique demonstrates the selective production of nanomaterials with high-quality output. Moreover, it yields impurity-free, clean, and homogeneous thin films, providing uniformity over a large substrate area [29-31]. This paper aims to synthesize Nb_2O_5 thin films by DC magnetron sputtering to make NO_2 gas sensors from Nb_2O_5/Si. Extensive investigations have explored the impact of sputtering power on the structure, morphology, optical characteristics, and sensing properties.

2. Experimental Work

Niobium oxide thin films were deposited on silicon wafers and quartz substrates using a DC reactive magnetron sputtering technique using various sputtering powers, specifically 25 W, 50 W, and 75 W. The primary aim was to investigate how the sputtering power affects the niobium oxide thin films' structural characteristics and surface morphology. The schematic representation of the experimental setup for the DC sputtering system is depicted in Fig. 1. The system comprises a glass vacuum chamber with dimensions of 30 cm in diameter and 25 cm in height. Within the chamber is a cathode in the form of a niobium target provided by Aldrich company, possessing a high purity level of 99.99%. The target has a diameter of 5 cm and a thickness of 3 mm, securely positioned at a distance of 5 cm from the anode. The target is electrically connected to a variable high-voltage DC power supply. Before deposition, the quartz substrates were thoroughly cleaned in an ultrasonic bath using isopropanol and deionized water, followed by drying with nitrogen gas. During the sputtering process, pure argon (99.99%) was utilized as the sputtering gas, while oxygen served as the reactive gas. The vacuum chamber was evacuated to a base pressure of 4.2×10^{-5} bar using a diffusion pump before sputtering. A mass flow controller was employed to introduce the reactive oxygen gas and argon sputtering gas into the vacuum chamber. The flow rate of the argon sputtering gas remained constant at 50 standard cubic centimeters per minute (sccm), while the oxygen flow rate was set to 5 sccm. The

deposition process lasted for 120 min. to fabricate the thin films. Subsequently, the thin films were annealed in ambient air at 800°C for 1 hr.

The gas sensor testing system is a custom-designed setup comprising a cylindrical stainless steel test chamber with specific dimensions. The chamber includes an inlet for introducing the tested gas and an air admittance valve to facilitate atmospheric airflow. Electrical connections for the heater, K-type thermocouple, and sensor electrodes are established through a multi-pin feedthrough at the base of the chamber. A heater, consisting of a hot plate and a K-type thermocouple, is employed to regulate and control the sensor's operating temperature. Sensing measurements are performed using a PC-interfaced digital multimeter (UNI-T 61E+) and a Laptop PC to record changes in sensor resistance when exposed to various gas mixing ratios, such as air-NO_2 gas. Gas flow is controlled using needle valves, enabling testing at different volumetric concentrations, particularly at a 3% gas-to-air ratio. A bias voltage of 6 volts is also applied across the two sides of the sensor's electrodes. The experimental investigation encompassed a temperature range spanning from 30 to 250 °C.

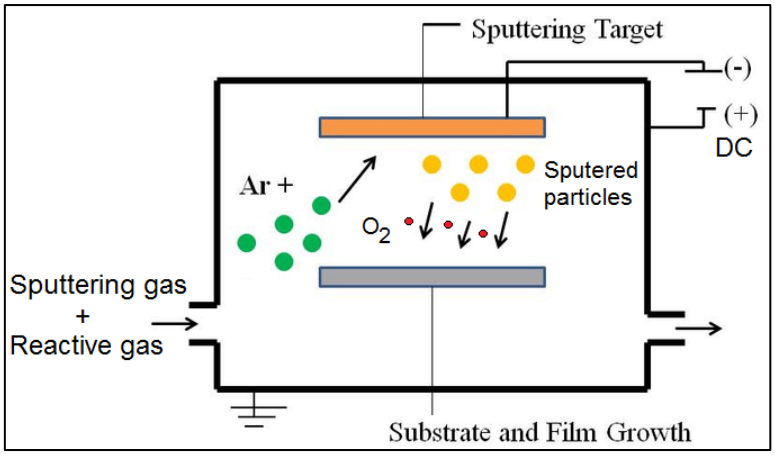

Figure 1: Illustrates a schematic representation of a DC sputtering system.

2.1 Characterization and Measurements

The crystalline structure of the produced sample was examined using "Shimadzu" XRD-6000 X-ray diffractometers, operating with CuK_α radiation (wavelength = 0.154 nm), within the 2θ range from 10° to 90°. Statistical and image analyses were performed using Image J and Origin LAB software, while quantitative analysis of elements was conducted using EDS (energy-dispersive X-ray spectroscopy). The UV-VIS spectrophotometer (Shimadzu UV-1650 PC) was used to take the readings of the optical absorption spectrum and the gap in optical energy of the deposited thin films in the wavelength range of 300–1100 nanometers. Hall effect measurements were carried out using the Van der Pauw method, utilizing the Ecopia HMS-3000 Hall Measurement Systems. The films' surface roughness and grain size distribution were analyzed using a high-resolution atomic force microscope (AFM) of the Angstrom Advanced Inc scanning probe microscope (model AA3000). Sensing measurements were conducted using a custom-built system.

3. Results and Discussion

3.1 X-Ray Diffraction Analysis

XRD analysis, as depicted in Fig. 2, was employed to investigate the structure and crystallinity of Nb_2O_5 films deposited on quartz substrates at various energies ranging from 25 W to 75 W with a step increment of 25 W. The XRD patterns revealed that all the films exhibited polycrystalline structures. Notably, diffraction peaks were observed

at 2θ angles of 22.431°, 28.819°, 36.805°, and 46.095°, corresponding to the (001), (100), (101), and (002) planes of hexagonal Nb_2O_5, in accordance with the JCPDS card number 00-028-0317 [32]. Additionally, the films displayed a significantly preferred orientation along the (001) diffraction peak, observed at a 2θ angle of 22.431°. The intensity of this preferred orientation steadily increased with the rise in DC sputtering power from 25 W to 75 W, particularly for the (001) and (100) planes, indicating an enhancement in the crystallinity of the Nb_2O_5 films. As the DC power was increased, the sample's crystalline quality exhibited enhancement, leading to the appearance of three diffraction lines associated with specific lattice planes: (110), (102), and (004), observed at diffraction angles of 50.674°, 55.187°, and 58.971°, respectively. Moreover, the broadening of the peaks in the diffraction lines indicated crystallite size increases directly with the DC power, which was evaluated by the Scherrer formula using the (001) diffraction line. The dimensions of the crystallite increase from 21.3 to 24.9 nm, with the DC power increasing from 25 to 75 W [33]. The crystallite sizes (D) associated with the most prominent peaks were measured and presented in Table 1. Additionally, Table 1 contains information on the peak positions and Miller indices for the diffraction planes, along with the corresponding full-width-at-half-maximum (FWHM) values. The obtained results align with previous investigations in the field [34].

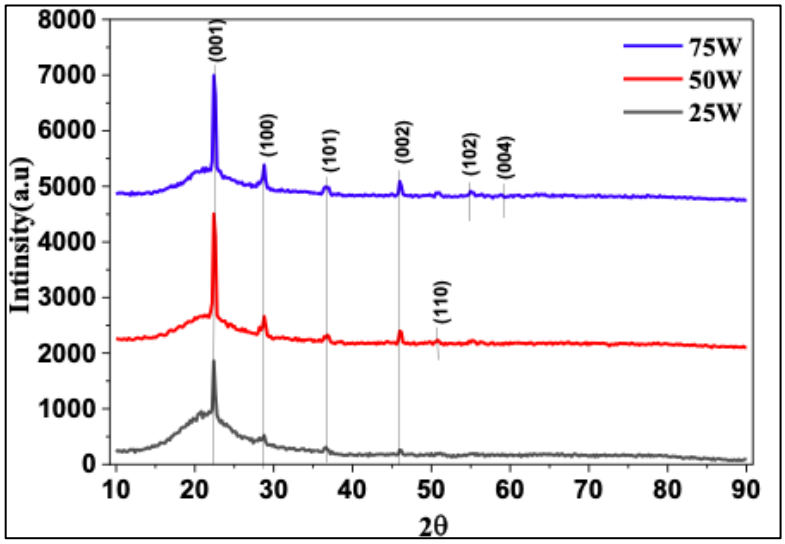

Figure 2: Nb_2O_5 thin film XRD patterns prepared at RT using different DC powers.

Table 1: XRD parameters of Nb_2O_5 thin film prepared at RT using different DC powers.

Power	2θ (Deg.)	FWHM (Deg.)	Relative Int.	d_{hkl} Exp.(Å)	D (nm)	d_{hkl} Std.(Å)	hkl
25	22.4046	0.3800	100.0	3.9650	21.3	3.9300	(001)
	28.7933	0.5324	6.7	3.0981	15.4	3.1200	(100)
	36.5927	0.6921	8.7	2.4537	12.1	2.4460	(101)
	46.1224	0.5058	8.1	1.9665	17.1	1.9620	(002)
50	22.4312	0.3727	100.0	3.9604	21.7	3.9300	(001)
	28.8199	0.4259	10.6	3.0953	19.3	3.1200	(100)
	36.8057	0.6758	5.6	2.4400	12.4	2.4460	(101)
	46.0958	0.4259	11.3	1.9676	20.3	1.9620	(002)
75	22.4046	0.3250	100.0	3.9650	24.9	3.9300	(001)
	28.7933	0.3461	9.0	3.0981	23.7	3.1200	(100)
	36.7524	0.6655	6.6	2.4434	12.6	2.4460	(101)
	45.9894	0.3992	13.9	1.9719	21.6	1.9620	(002)

3.2 Optical Properties

By employing Eq. (1), it becomes possible to calculate the absorption coefficient directly for the specific frequency linked to the high absorption region. This calculation entails utilizing the values of absorption (A) and thickness (t) to determine the coefficient [35]

$$\alpha = 2.303\frac{A}{t} \quad (1)$$

The distinct characteristic of crystalline and amorphous materials is evident in their fundamental absorption edges. To ascertain the material's band gap, it is essential to comprehend the transition from the valence band to the conduction band. The calculation of the energy band gap (E_g) is performed according to Eq.(2) [36, 37].

$$\alpha h\nu = B(h\nu - E_g)^r \quad (2)$$

In the given equation, the constant B is determined by the specific structural characteristics of the material. The variable h corresponds to the Planck constant, whereas ν denotes the frequency of the incident photons. Additionally, the equation incorporates the optical energy gap, represented by E_g, and the index r, which characterizes the particular optical absorption process involved. The value of r can be 1/2, 3/2, 2, or 3, depending on the type of electronic transition responsible for the absorption phenomenon [38, 39]. UV-Visible spectra determined the absorption coefficient for different wavelengths of electromagnetic radiation. For the calculation, a value of 0.5 was selected for the r-coefficient, representing allowed direct optical transitions. In Fig. 3, the optical absorbance properties of Nb_2O_5 thin films are depicted as they are deposited at room temperature (RT) using different DC powers within the 200-800 nm wavelength range. The thin films exhibit high absorbance in the UV range but demonstrate low absorbance in the visible wavelength region. With an increase in the DC power, there is a corresponding rise in the absorbance attributed to the increased thickness of the thin films and enhanced sputtering yield, indicating a reduction in lattice defects and the elimination of tail states near the band edges [40].

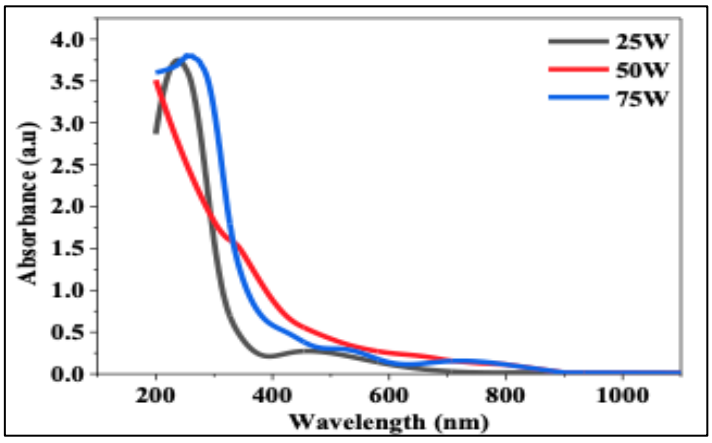

Figure. 3: UV-VIS optical absorbance for the Nb_2O_5 thin films prepared at the RT by different DC powers.

Fig. 4 illustrates the relationship between $(\alpha h\upsilon)^2$ and photon energy ($h\upsilon$) for Nb_2O_5 thin films prepared at RT with different DC powers. The band gap value was obtained by extrapolating the tangential linear curve to the x-axis. An interesting observation was made regarding decreased direct optical energy gap as the DC power increased. This decrease can be attributed to the enlarged size of the crystallites, as

validated by the X-ray diffraction analysis. The increase in crystallite size reduces the quantum confinement effect, which becomes more prominent at the nano-scale. Previous studies have also reported this trend of decreasing the optical energy gap with increasing DC power. The band gap values obtained in this research align with those reported in the referenced literature [41, 42].

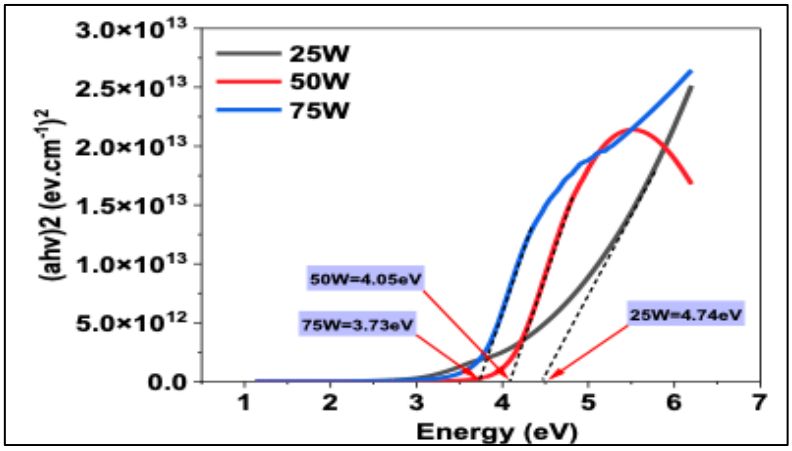

Fig 4: $(\alpha h\upsilon)^2$ versus $(h\upsilon)$ for Nb_2O_5 thin films prepared at the RT by different DC powers.

3.3 Atomic Force Microscopy

The three-dimensional (3D) AFM images and the cumulative histogram illustrate the particle size distribution on the surface of Nb_2O_5 thin films deposited on quartz substrates at RT using different sputtering powers (25, 50, and 75 W) as shown in Fig. 5. The AFM images prove that a consistent and uniform surface texture characterizes the Nb_2O_5 films deposited using DC sputtering. Furthermore, the particle size increases from (35.81) to (45.56) nm with increasing the DC power from 25 to 75 W, while at a DC power of 50 W, the particle size measures (41.86) nm. Surface roughness plays a significant role in determining the gas-sensing performance of the samples. The samples prepared at RT using 75 W of DC power exhibited the highest surface roughness among all the tested conditions. These findings are consistent with a previously reported study, further supporting the importance of surface roughness in gas-sensing applications [42, 43].

3.4 EDX Analysis

Energy-dispersive X-ray spectroscopy (EDX) was utilized to perform a quantitative analysis of the elements. The operating principle of EDX is based on the unique electromagnetic emission spectra exhibited by each element following X-ray excitation. Fig. 6 illustrates the atomic percentages of Nb and O in Nb_2O_5 thin films deposited at different powers. As depicted in Fig. 6, raising the DC sputtering power led to a greater sputtering yield, consequently causing an escalation in the Nb content from 12.2 at.% to 20.1 at.% [44]. This increase in power leads to the ejection of a more significant number of Nb atoms from the target material (Nb_2O_5), consequently raising the Nb content in the deposited thin films. Conversely, the lower O weight percentage is attributed to a relatively smaller proportion of oxygen atoms being incorporated into the films compared to the increasing Nb atoms. The noted changes in weight ratios offer a significant understanding regarding the impact of deposition power on the oxygen-to-metal content.

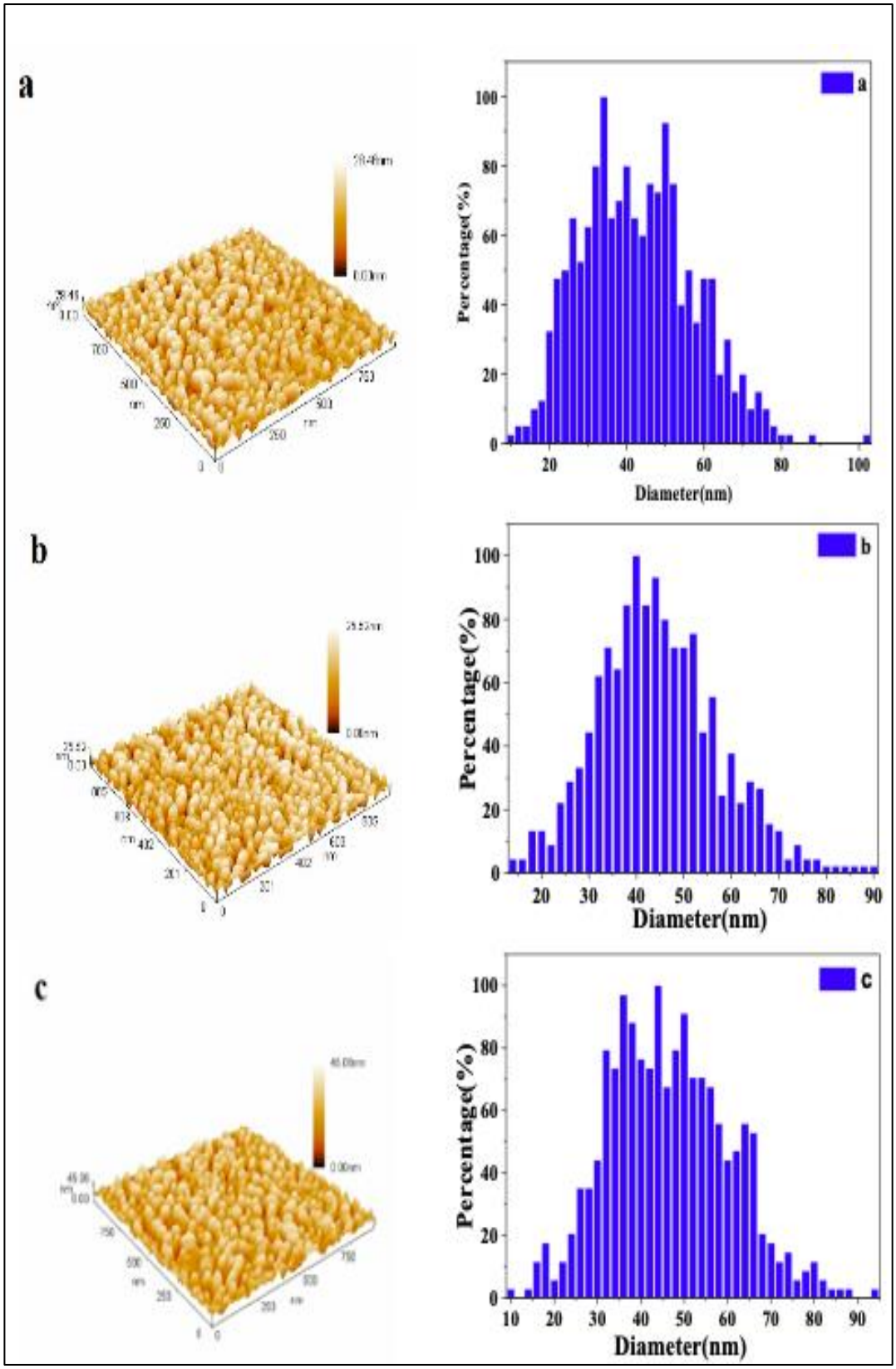

Figure 5: Three-dimensional atomic force microscopy (3D AFM) and size distributions for Nb_2O_5 thin films at different sputtering DC powers: (a) 25 W, (b) 50 W, and (c) 75W.

3.5 Hall Effect Measurements

Hall measurements were utilized to analyze the charge carriers, concentration (n_H), and Hall mobility (μ_H) of Nb_2O_5 thin films deposited at various power levels. The

results indicated that all samples exhibited n-type behavior, as indicated by the negative sign of R_H. The mobility of charge carriers in these films is influenced by grain boundaries, which are abundant and contain defects due to the disorganized arrangement of atoms. These defects act as barriers hindering the movement of charge carriers between grains, with the barrier height dependent on the grain size [45]. Increasing the sputtering power from 25 to 75 W resulted in higher carrier mobility, which can be attributed to the larger grain size. This observation is consistent with previous findings in the literature [46]. Conversely, the decrease in concentration (n_H) is attributed to the inverse relationship between μ_H and $n_{H,}$ as shown in Table 2.

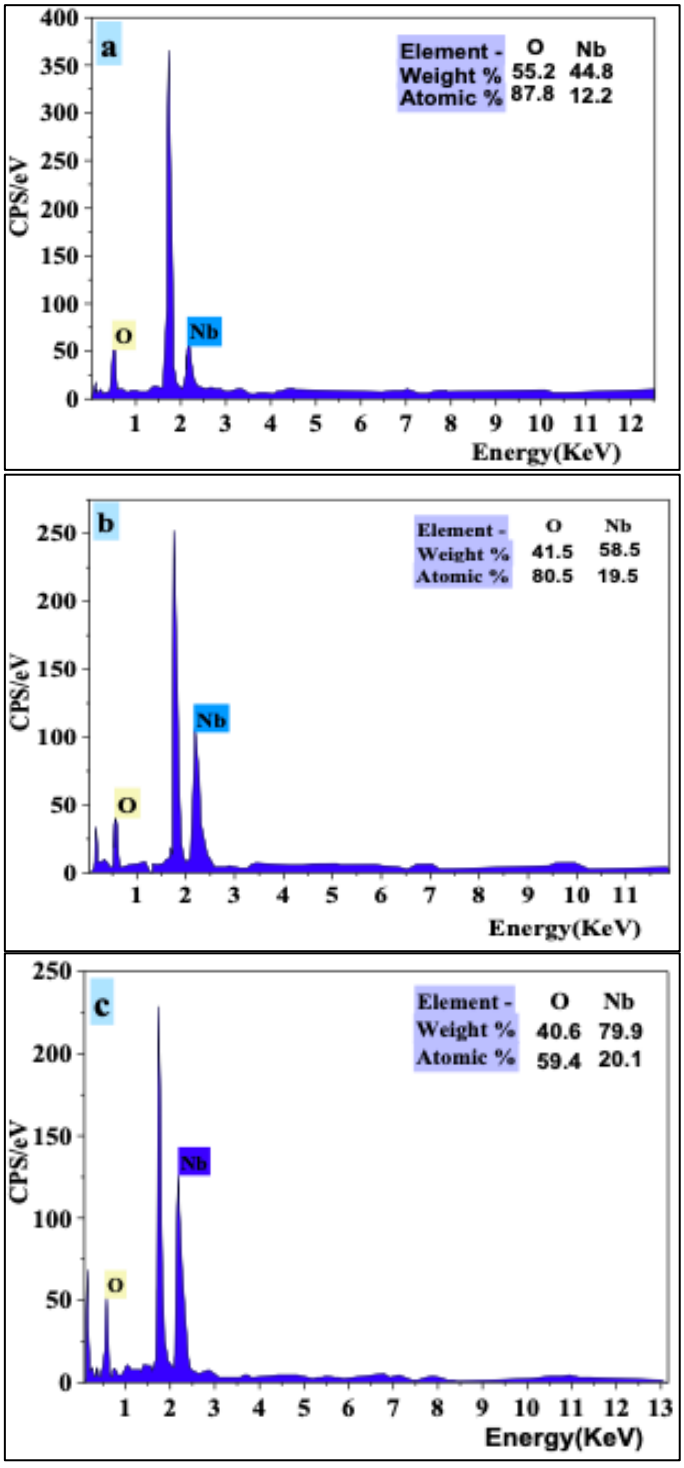

Figure 6: EDS results for Nb_2O_5 thin films prepared at RT by different DC powers: (a) 25 W, (b) 50 W, and (c) 75 W.

Table 2: Hall effect measurements for Nb_2O_5 thin films prepared at RT by different DC powers.

Power (W)	$n\times10^{12}$ (cm^{-3})	μ_H (cm^2/v.sec)	σ_{RT} ($\Omega^{-1}.cm^{-1}$)	Type
25	17.11	33.97	9.30E-05	n-type
50	7.68	237.40	2.92E-04	n-type
75	2.91	682.10	3.18E-04	n-type

3.6 Gas Sensing Measurement

The sensor's sensitivity was evaluated using Eq. (3) and the calculation approach outlined in reference [47].

$$S = \left|\frac{(R_g - R_a)}{R_a}\right| \times 100\%, \qquad (3)$$

where S represents the sensitivity, R_a and R_g represent the electrical resistance of the film when measured in the air and the presence of gas, respectively [48]. The experiment used a constant concentration of NO_2 target gas, kept explicitly at 3% in atmospheric air throughout the study.

3.7 Gas Sensing Mechanism of Nb_2O_5 Thin Films

The changes in resistance over time were studied by exposing the samples to NO_2 gases using an on/off gas valve. The samples in question comprised Nb_2O_5 thin films deposited on silicon wafers using DC reactive magnetron sputtering. The sputtering powers employed during the deposition process ranged from 25 to 75 W, while the experiment covered a range of operating temperatures from 30 to 250 °C. Oxygen molecules get adsorbed from the surrounding atmosphere on the sensor's active surface. These molecules then become ionized by losing electrons from the conduction band of the sample surface. This process results in the formation of a surface depletion layer and different types of oxygen ions [49]. The depth of the depletion layer depends on the quantity of adsorbed gases, creating potential barriers that hinder the movement of charge carriers through the channels between adjacent nanoparticles. When oxidizing gases come into contact with the surface of the sample, they have the tendency to extract electrons, leading to a reduction in the charge carrier concentration and mobility. This interaction causes a change in the depth of the surface depletion layers. Consequently, the resistance of the sample increases when exposed to oxidizing gases [50]. Fig. 7 shows the variation of resistance as a function of time with an on/off gas valve. The resistance increases when the gas valve is on. However, the resistance decreases rapidly when the gas is off because NO_2 is an oxidizing gas.

3.8 Determination of the Operating Temperature for the Sensor

Fig. 8 illustrates the gas sensitivity of different Nb_2O_5 thin film samples fabricated using DC sputtering. The sensitivity, measured in relation to the presence of NO_2 gas, is plotted against the operating temperature. The observed variations in sensitivity at different temperatures can be attributed to the diverse types and amounts of oxygen species that are adsorbed on the surface of the samples. These oxygen species play a critical role in the gas sensitivity mechanisms [30]. The maximum sensitivity appeared at 200°C against the NO_2 gas for the sample prepared at a power of 50 W. The deposition conditions have a substantial influence on the gas sensitivity of thin films, which is consistent with previous research findings. This can be attributed to factors like the roughness of the sample surfaces and the connection among the grains. Furthermore, the presence of oxygen vacancies is a critical factor in determining the sensitivity of the samples.

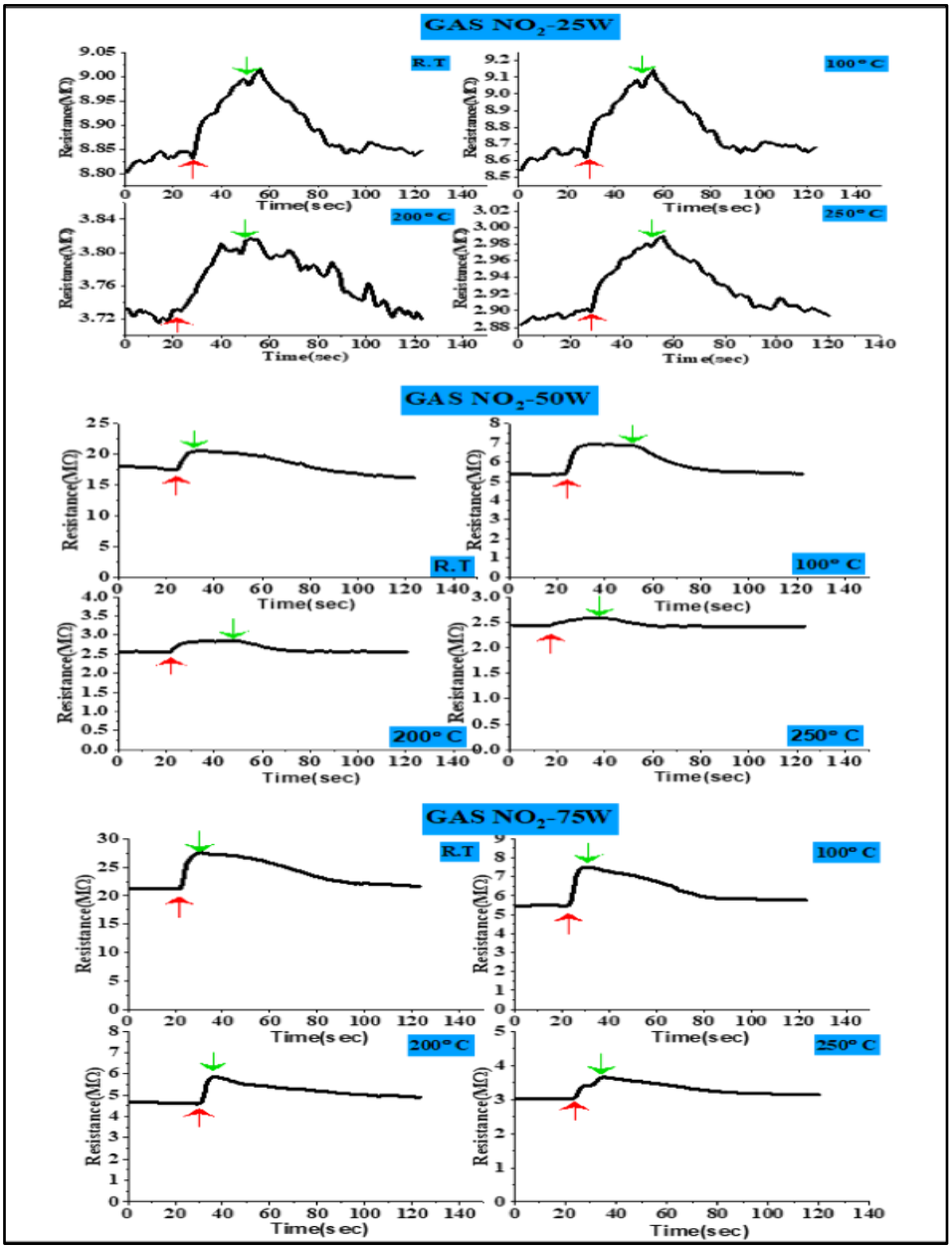

Fig. 7: Resistance as a function of time for different temperatures (RT,100,200, and 250°C) for Nb_2O_5 thin films prepared at RT by different DC powers: 25, 50, and 75 W.

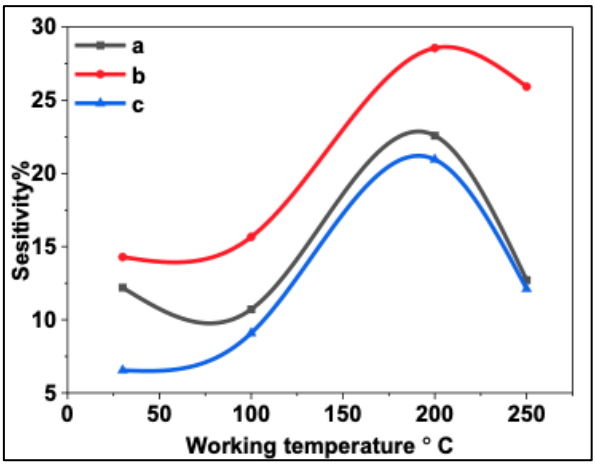

Figure 8: NO_2 gas sensitivity versus working temperature for Nb_2O_5 thin films prepared by different DC powers: (a) 25 W, (b) 50 W, and (c) 75 W.

3.9 Response Time and Recovery Time

The response time of a gas sensor refers to the duration needed for the sensor's conductance to reach 90% of its maximum or minimum value when introducing a reducing or oxidizing gas, respectively. This is expressed in Eq. (4). Similarly, the recovery time signifies the time it takes for the sensor's conductance to return to within 10% of the initial baseline level after the gas flow is stopped, as indicated in Eq. (5) [51].

$$response\ time = \left|t_{gas(on)} - t_{gas(off)}\right| \times 0.9 \quad (4)$$

$$recovery\ time = \left|t_{gas(off)} - t_{gas(recovery)}\right| \times 0.9 \quad (5)$$

Fig. 9 presents the relationship between the response time and recovery time of Nb_2O_5 thin films at different operating temperatures. The deposition process involved using a 3% NO_2: air mixing ratio on a p-type Si wafer (100). The graph demonstrates a rapid response time of 10 seconds and a recovery time of 40 seconds. This indicates that the NO_2 gas sensor exhibits a prompt response when a sufficient quantity of gas is present for the desired reaction to occur. The longer recovery time compared to the response time in gas sensors is primarily attributed to the desorption process. Upon detecting a target gas and initiating a response, the gas molecules become adsorbed on the sensor's surface, leading to changes in its electrical properties. However, once the gas is no longer present, the sensor requires time to release or desorb the gas molecules from its surface and return to its initial state [52, 53]. Table 3 shows the response, recovery times, and sensitivity % for NO_2 gas at four operator temperatures (RT, 100, 200, and 250) ^{o}C for Nb_2O_5 thin films at various sputtering powers.

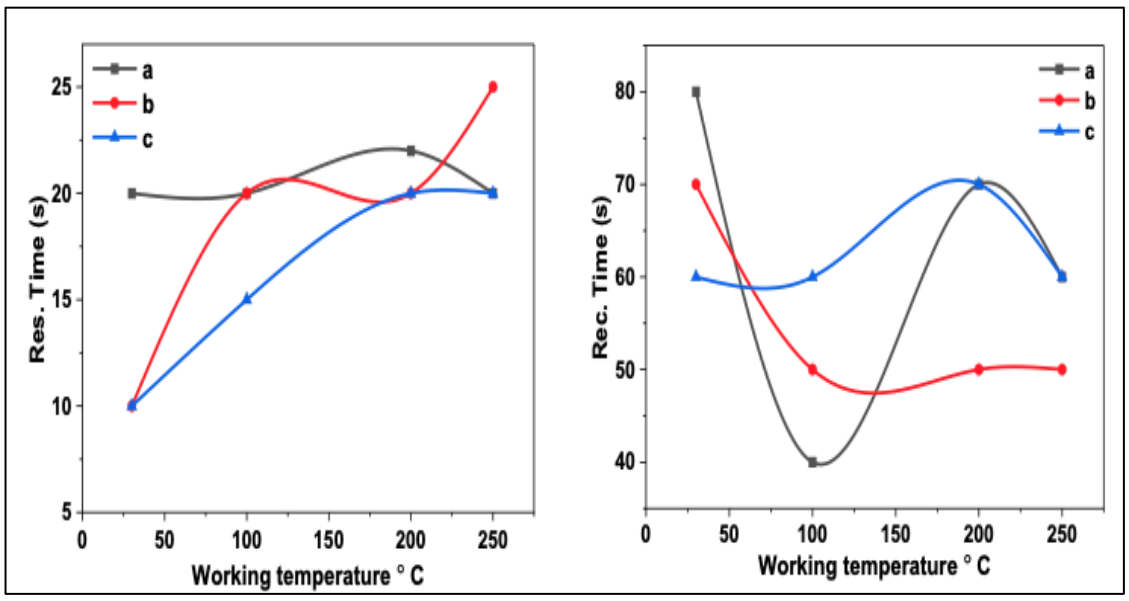

Figure 9: The relationship between the response time, recovery time, and operating temperature for Nb_2O_5 thin films at various sputtering powers: (a) 25 W, (b) 50 W, and (c) 75 W.

Table 3: Response, recovery times, and sensitivity % for Nb_2O_5 thin films at various sputtering powers.

Power (W)	Temp. (ºC)	NO_2 Sensitivity%	Res. Time (s)	Rec. Time (s)
25	**RT**	12.2	23.0	78.0
	100	10.7	21.0	40.0
	200	22.6	22.0	71.0
	250	12.7	18.0	59.0
50	**RT**	14.3	10.0	72.0
	100	15.7	18.0	48.0
	200	28.6	19.0	47.0
	250	25.9	25.0	51.0
75	**RT**	6.5	12.0	61.0
	100	9.1	15.0	58.0
	200	21.0	22.0	72.0
	250	12.1	21.0	60.0

4. Conclusions

This research study successfully utilized the widely adopted sputtering technique to produce high-quality Nb_2O_5 thin films. XRD analysis confirmed the polycrystalline structure of the films, exhibiting a hexagonal phase. Notably, increasing the DC power during deposition resulted in a decrease in the direct optical energy gap. Furthermore, the average diameter of the films increased with higher sputtering power. The NO_2 gas sensor, fabricated with a power of 50 W, exhibited an impressive sensitivity of 28.6% at RT. Additionally, this sensor demonstrated a rapid response time of 10 seconds under the same power setting. The fastest recovery time of 40 seconds was observed for the sample prepared with a power of 25 W.

Acknowledgments

The authors would like to thank University of Baghdad, College of Science, Department of Physics for supporting the research.

Conflict of interest

The authors declare that they have no conflict of interest.

References

1. C. Nico, T. Monteiro, and M. P. Graça, Prog. Mat. Sci. **80**, 1 (2016).
2. G. H. M. Gomes and N. D. Mohallem, Mat. Lett. **318**, 132136 (2022).
3. K. Islam, R. Sultana, B. Satpati, and S. Chakraborty, Vacuum **195**, 110675 (2022).
4. J. Lin, S. Zhao, T. G. Tranter, Z. Zhang, F. Peng, D. Brett, R. Jervis, and P. R. Shearing, Electrochim. Act. **443**, 141983 (2023).
5. W. Elshirbeeny, M. Harthy, and A. Alshahrie, Int. J. Opt. Photonic. Eng. **4**, 019 (2019).
6. L. Yang, Y. Wei, Y. Song, Y. Peng, Y. Yang, and Z. Huang, Mat. Des. **193**, 108808 (2020).
7. J. M. Hwang, N. Y. Kim, S. Shin, J. H. Lee, J. Y. Ryu, T. Eom, B. K. Park, C. G. Kim, and T.-M. Chung, Polyhedron **200**, 115134 (2021).
8. A. C. S. Valentim, E. O. Da Silva, P. S. R. C. Da Silva, D. S. Garcia, and M. I. B. Tavares, Poly. Tes. **70**, 111 (2018).
9. Z. Liu, W. Dong, J. Wang, C. Dong, Y. Lin, I.-W. Chen, and F. Huang, Iscience **23**, (2020).

10. A. Golobič, A. Meden, M. Spreitzer, and S. Škapin, J. Eur. Ceram. Soci. **41**, 7035 (2021).
11. R. Lan, J. T. Irvine, and S. Tao, Int. J. Hyd. Ener. **37**, 1482 (2012).
12. F. Schüth, R. Palkovits, R. Schlögl, and D. S. Su, Ener. Envir. Sci. Tech. **5**, 6278 (2012).
13. S. W. Lee, W. Lee, Y. Hong, G. Lee, and D. S. Yoon, Sen. Actuat. B: Chem. **255**, 1788 (2018).
14. T. Takeuchi, H. Takahashi, K. Saji, H. Kondo, and I. Igarashi. 1983, SAE Technical Paper: Tokyo, Japan. pp. 627
15. L. Chambon, J. Germain, A. Pauly, V. Demarne, and A. Grisel, Sens. Actuat. B: Chem. **60**, 138 (1999).
16. A. Eftekhari and P. Corrochano, Sust. Ener. Fuel. **1**, 1246 (2020).
17. O. A. Jassim, M. M. Mutter, and S. Khalil, in Materials Science Forum, Trans Tech Publ, 2022, p. 21.
18. W. Ai and S. Xiong, Opt. Laser Tech. **150**, 107850 (2022).
19. X. Lv, Y. Wei, G. Liu, Z. Huang, and Y. Yang, Ceram. Int. **49**, 10395 (2023).
20. S. Pat, Ö. Çelik, A. Odabaş, and Ş. Korkmaz, Optik **258**, 168928 (2022).
21. R. Siripuram, P. Rao, and S. Sripada, Physics
Chem. Glasses-Eur. J. Glass Sci. Tech. Part B **63**, 65 (2022).
22. I. M. Ali and I. M. Ibrahim, Iraqi J. Phys. **19**, 20 (2021).
23. M. Z. Iqbal, M. Alzaid, U. Abbasi, S. Alam, R. Ali, A. M. Afzal, and S. Aftab, Int. J. Ener. Res. **46**, 7334 (2022).
24. A. M. Koshy, A. Sudha, S. K. Yadav, and P. Swaminathan, Phys. B: Conden. Matt. **650**, 414452 (2023).
25. S. B. Q. Tran, F. Y. Leong, R. Hariharaputran, D. Wenjun, P.-Y. Lai, and D. V. Le, Vacuum **213**, 112097 (2023).
26. S. Abd Al Kareem and W. Yaseen, in IOP Conference Series: Materials Science and Engineering, IOP Publishing, 2020, p. 012054.
27. M. A. Butt, C. Tyszkiewicz, P. Karasiński, M. Zięba, A. Kaźmierczak, M. Zdończyk, Ł. Duda, M. Guzik, J. Olszewski, and T. Martynkien, Materials **15**, 4591 (2022).
28. F. Chen, Y. Zhou, Y. Zhu, R. Zhu, P. Guan, J. Fan, L. Zhou, N. Valanoor, F. Von Wegner, and E. Saribatir, J. Mat. Chem. C **9**, 8372 (2021).
29. K. Yahya, Iraqi J. Phys. **15**, 202 (2017).
30. F. Challali, D. Mendil, T. Touam, T. Chauveau, V. Bockelée, A. G. Sanchez, A. Chelouche, and M.-P. Besland, Mat. Sci. Semicond. Proces. **118**, 105217 (2020).
31. M. Rudolph, N. Brenning, M. A. Raadu, H. Hajihoseini, J. T. Gudmundsson, A. Anders, and D. Lundin, Plas. Sour. Sci. Tech. **29**, 05LT01 (2020).
32. E. I. García-López, F. R. Pomilla, B. Megna, M. L. Testa, L. F. Liotta, and G. Marcì, Nanomaterials **11**, 1821 (2021).
33. M. Imran, R. Ahmad, N. Afzal, and M. Rafique, Vacuum **165**, 72 (2019).
34. A. M. Al-Baradi, M. El-Nahass, A. Hassanien, A. Atta, M. S. Alqahtani, and A. O. Aldawsari, Optik **168**, 853 (2018).
35. A. F. Rauuf and K. A. Aadim, Iraqi J. Sci. **64**, 2877 (2023).
36. K.-N. Chen, C.-M. Hsu, J. Liu, Y.-C. Liou, and C.-F. Yang, Micromachines **7**, 151 (2016).
37. E. Davis and N. Mott, Philosoph. Mag. **22**, 0903 (1970).
38. H. Hou, Z. Jun, A. Reuning, A. Schaper, J. Wendorff, and A. Greiner, Macromolecules **35**, 2429 (2002).
39. G. Ma, Y. Dongzhi, and N. Jun, Poly. Advan. Tech. **20**, 147 (2009).
40. S. Xu and Z. L. Wang, Nano Res. **4**, 1013 (2011).

41. R. A. Rani, A. S. Zoolfakar, A. P. O'mullane, M. W. Austin, and K. Kalantar-Zadeh, J. Mat. Chem. A **2**, 15683 (2014).
42. Ö. D. Coşkun, S. Demirel, and G. Atak, J. All. Comp. **648**, 994 (2015).
43. N. Usha, R. Sivakumar, C. Sanjeeviraja, and M. Arivanandhan, Optik-Int. J. Light Elec. Opt. **126**, 1945 (2015).
44. A. Atta, A. Hassanien, M. El-Nahass, A. A. Shaltout, Y. A. Al-Talhi, and A. M. Aljoudi, Opt. Quan. Elec. **51**, 1 (2019).
45. E. T. Salim, J. A. Saimon, M. K. Abood, and M. A. Fakhri, Mat. Res. Expres. **6**, 126459 (2020).
46. A. Ibraheam, J. M. Rzaij, M. A. Fakhri, and A. Abdulwahhab, Mat. Res. Expres. **6**, 055916 (2019).
47. L. A. Patil, A. R. Bari, M. D. Shinde, V. V. Deo, and D. P. Amalnerkar, IEEE Sen. J. **11**, 939 (2010).
48. L. Fan, X. Yang, and H. Sun, J. Mat. Chem. C **11**, 10163 (2023).
49. A. Staerz, U. Weimar, and N. Barsan, Sen. Actuat. B: Chem. **358**, 131531 (2022).
50. J. Hsieh, C. Liu, and Y. Ju, Thin Sol. Fil. **322**, 98 (1998).
51. N. K. Abbas, I. M. Ibrahim, and M. A. Saleh, Silicon **10**, 1345 (2018).
52. S. Pagidi, K. S. Pasupuleti, M. Reddeppa, S. Ahn, Y. Kim, J.-H. Kim, M.-D. Kim, S. H. Lee, and M. Y. Jeon, Sen. Actuat. B: Chem. **370**, 132482 (2022).
53. M. K. Khalaf, B. T. Chiad, A. F. Ahmed, and F. a. H. Mutlak, Int. J. Appl. Innov. Eng. Manag. **2**, 178 (2013).

تأثير طاقة الترذيذ المغناطيسي بالتيار المستمر على الخصائص التركيبية والمورفولوجية وخصائص المتحسس الغازي لأغشية Nb_2O_5/Si الرقيقة

يحيى رشيد هذال[1]، عصام محمد ابراهيم[1]، محمد خماس خلف[2]، احسان حميان صبار[3]، ومسارع كريم محمود[4]

[1]قسم الفيزياء، كلية العلوم، جامعة بغداد، بغداد، العراق

[2] دائرة بحوث المواد، وزارة العلوم والتكنولوجيا، بغداد، العراق

[3]قسم الهندسة الكهربائية، جامعة الانبار، الرمادي، العراق

[4]قسم هندسة أنظمة الطاقة، جامعة أنقرة يلدريم بيازيد، ، تركيا

الخلاصة

تركز هذه الدراسة على تصنيع أغشية رقيقة من خامس أوكسيد الفناديوم (Nb_2O_5) باستخدام الترذيذ المغناطيسي المتفاعل بتيار مستمر لأجل تحسس غاز NO_2. تخضع الأفلام لعملية تلدين في الهواء المحيط عند درجة حرارة 800 درجة مئوية لمدة ساعة واحدة. يتم استخدام تقنيات متعددة للتوصيف، بما في ذلك حيود الأشعة السينية (XRD)، والفحص المجهري للقوى الذرية (AFM)، والتحليل الطيفي للأشعة السينية المشتتة للطاقة (EDS)، وقياسات تأثير هول، وقياسات التحسسية، لتقييم الخصائص الهيكلية والمورفولوجية والكهربائية والاستشعارية لأغشية Nb_2O_5 الرقيقة. يؤكد حيود الأشعة السينية ان للأغشية طبيعة متعددة البلورات والبنية البلورية السداسية لـ Nb_2O_5. يتم تقدير المعلمات البصرية، مثل الامتصاص البصري وطاقة فجوة النطاق، لتوصيف الخصائص البصرية للأفلام. تشير صور AFM إلى زيادة في متوسط القطر مع زيادة قوة الترذيذ. تكشف تحاليل EDS عن زيادة في نسبة Nb مع زيادة قوة الترذيذ. تُظهر قياسات تأثير هول أن جميع الأفلام من نوع n، وأن زيادة قوة الترذيذ تؤدي إلى انخفاض تركيز الناقل وزيادة القابلية للتحرك. تم تقييم حساسية المستشعر للغاز وزمن الاستجابة وزمن الاسترداد عند درجات حرارة تشغيل متعددة. أظهر استشعار NO_2 حساسية مثلى قدرها 28.6% عند 200 درجة مئوية عند ضبط قوة الترذيذ على 50 واط.

الكلمات المفتاحية: خامس أوكسيد الفناديوم، الترذيذ، مطيافية تشتت الطاقة، التحسسية، ثنائي أوكسيد النتروجين.